Snow Avalanche Detection and Mapping in multitemporal and multiorbital Radar Images from TerraSAR-X and Sentinel-1

Silvan Leinss[*1], Raphael Wicki[*1], Sämi Holenstein[1], Simone Baffelli[1], and Yves Bühler[2]

[*]These authors contribute equally to the paper
[1]Institute of Environmental Engineering, ETH Zurich, Zurich, Switzerland
[2]WSL-Institute for Snow and Avalanche Research SLF, Davos Dorf, Switzerland

Correspondence: Silvan Leinss (leinss@ifu.baug.ethz.ch)

Abstract. Snow avalanches can endanger people and infrastructure, especially in densely populated mountainous regions. In Switzerland, the public is informed by an avalanche bulletin issued twice a day during winter which is based on weather information and snow and avalanches reports from a network of observers. During bad weather, however, information about occurred avalanches can be scarce or even be missing completely. To asses the potential of weather independent radar satellites we compared manual and automatic change detection avalanche mapping results from high resolution TerraSAR-X (TSX) stripmap images and medium resolution Sentinel-1 (S1) interferometric wide swath images for a study site in central Switzerland. The TSX results were also compared to available mapping results from high-resolution SPOT-6 optical satellite images. We found that avalanche outlines from TSX and S1 agree well with each other. Cut-off thresholds of mapped avalanche areas of 500 m^2 for TSX and 2000 m^2 for S1 were found. S1 provides a much higher spatial and temporal coverage and allows for mapping of the entire Alps at least every 6 days with freely available acquisitions. With costly SPOT-6 images the Alps can be even covered in a single day at meter-resolution, at least for clear sky conditions. For the SPOT-6 and TSX mapping results we found a fair agreement but the temporal information from radar change detection allows for a better separation of overlapping avalanches. Still the total mapped avalanche area differed by at least a factor of three because with radar, mainly the avalanche deposition zone was detected, whereas the release zone was well visible already in SPOT-6 data. With automatic avalanche mapping we detected around 70 % of manually mapped new avalanches, at least when the number of old avalanches is low. To further improve the radar mapping capabilities, we combined S1 images from multiple orbits and polarizations and obtained a notable enhancement of resolution and speckle reduction such that the obtained mapping results are almost comparable to the single orbit TSX change detection results. In a multiorbital S1 mosaic covering entire Switzerland, we manually counted 7361 new avalanches which occurred during an extreme avalanche period around Jan 4th 2018.

1 Introduction

Snow avalanches frequently threaten people and infrastructure in Switzerland and other mountainous countries. Every winter, dozens of people caught in avalanches suffer serious injuries or even die (Techel et al., 2016) and roads and railways have to be closed during periods of high avalanche danger. To inform about the current avalanche danger levels, ranging from 1 (low) to 5 (very high) on the European Avalanche Hazard Scale (Meister, 1995), the WSL-Institute for Snow and Avalanche Research (SLF) publishes an avalanche bulletin twice a day during winter (SLF, 2018e). The bulletin is written by avalanche experts which analyze weather station data, local snow conditions, detailed weather forecast information and avalanche occurrence reported by a network of in-situ observers. Unfortunately during high avalanche activity low visibility and closed valleys and ski resorts can lead to incomplete or missing avalanche occurrence information. In such situations, as happened in Switzerland in January 2018 and 2019, avalanches can be mapped manually in optical airborne images (Bühler et al., 2009; Eckerstorfer et al., 2016; Korzeniowska et al., 2017) or satellite images which have to be tasked in rapid mapping mode (Scott, 2009; Lato et al., 2012; Bühler et al., 2019). The resulting avalanche outlines can then be used to update avalanche databases which are of great value for hazard mapping and mitigation measure planning (Rudolf-Miklau et al., 2014). As manual mapping is very time-consuming, attempts have been made to automatize avalanche mapping in optical data (Bühler et al., 2009; Lato et al., 2012; Frauenfelder et al., 2015; Korzeniowska et al., 2017). To provide weather-independent observations the project Alpine Avalanche Forecast service (AAF) evaluated terrestrial and spaceborne radar images (Bühler et al., 2014). They concluded that medium to large avalanche events could be mapped using very high resolution radar satellites but with the drawbacks of limited availability and high costs. Nevertheless, for freely available but medium-resolution Sentinel-1 radar images few but promising manual and automatic avalanche mapping studies exist (Vickers et al., 2016; Eckerstorfer et al., 2017; Wesselink et al., 2017; Abermann et al., 2019; Eckerstorfer et al., 2019).

To evaluate the applicability of high and medium resolution radar images for avalanche detection in the Swiss Alps we compare 10-meter resolution Sentinel-1 radar images, 3-meter resolution TerraSAR-X radar images, and 1.5 meter resolution SPOT-6 optical images and analyze different methods using multitemporal and multiorbital radar images for two extreme avalanche events which occurred in Switzerland in Jan 2018.

2 Study area and data

The study area, shown in Fig. 1, was determined by the spatial and temporal availability of high resolution radar images from the satellite TerraSAR-X (TSX), operated by the German Aerospace Center (DLR). No systematic TSX coverage is available over Switzerland because data are acquired upon request (Werninghaus and Buckreuss, 2010). To cover the two extreme avalanche events around Jan 4th and 22nd 2018 (Fig. 2) with images acquired from identical orbits as good as possible we searched the archive for a sequence of images which limited the study area to the Alps of Uri in central Switzerland. The orbit repeat time defines the dates and limits the revisit time to 11 days for the first event and 22 days for the second one (one acquisition missing). The images were acquired in X-band (9.6 GHz) with the standard TSX stripmap mode (SM) at a nominal single-look complex (slc) resolution of 2.3×3.3 m (rg$\times$az). Acquisitions are listed in Table 1. Snow and weather conditions

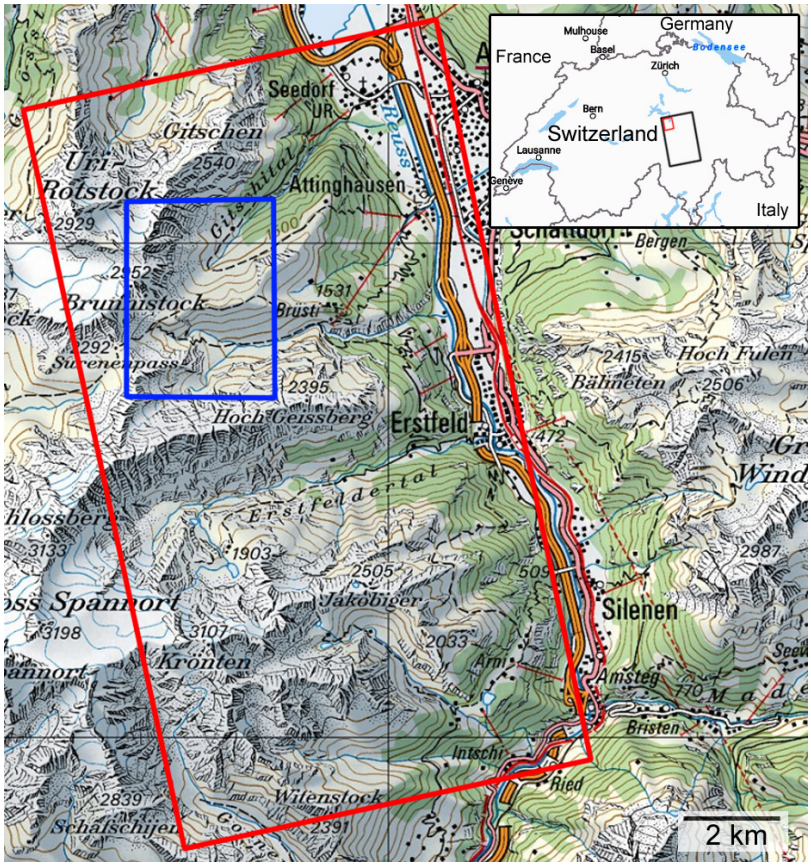

Figure 1. Area selected for avalanche mapping (Red rectangle). Blue rectangle: subset used to visualize radar images and mapping results (46°51' N, 8°34' E). The black rectangle in the insets shows the full footprint of the TSX scene over Switzerland. © 2019 swisstopo (JD100042), reproduced with the authorisation of swisstopo (JA100120).

during the two avalanche events are summarized by Bühler et al. (2019). Details are provided by Winkler et al. (2019) and SLF (2018a, b, c, d) (in German).

The full TSX scene (black rectangle in the inset in Fig. 1) covers $55\times35\,\mathrm{km}^2$ but for the analysis we selected an area of $15.3\times8.6\,\mathrm{km}^2$ (red rectangle in Fig. 1) where both the TSX and the validation data (Bühler et al., 2019) show a very high avalanche activity. The selected area contains steep topography which ranges from 400 - 3200 m.a.s.l.. For visualization of results we show in the following only a small subset (blue rectangle in Fig. 1) of the analyzed area.

Radar images of the satellite Sentinel-1 (S1) were analyzed for comparison. S1 images are acquired globally and systematically and are free and openly available for download within 24 hours after acquisition (ESA, 2012). Currently, S1 consists of two satellites, S1-A and S1-B, which alternately image central Europe every six days from the same orbit with an slc resolution of 2.7×22.5 m (rg$\times$az) in the interferometric wide swath mode (IW). The S1 images, covering $250\times170\,\mathrm{km}^2$, were selected such that they had orbits and acquisition times similar to TSX.

Table 1. Satellite data with local acquisition time (CET = UTC+1). Acquisition modes are abbreviated as SM (stripmap), IW (interferometric wide swath), and MS (single pass multi-strip collection). The full list of S1 acquisitions used for the composite of Switzerland is listed in Table A1.

satellite	date, time (CET)	mode	pol. / band	aoi	orbit
TSX	2017-12-31 18:09	SM	HH	29°	40 asc
TSX	2018-01-11 18:09	SM	HH	29°	40 asc
TSX	2018-02-02 18:09	SM	HH	29°	40 asc
S1	2017-12-31 18:14	IW-1	VV,VH	34°	15 asc
S1	2018-01-12 18:14	IW-1	VV,VH	34°	15 asc
SPOT-6	2018-01-24 10:03	MS	R,G,B,NIR	3.1°	

The first analyzed images of both satellites were acquired on 2017-12-31 a few minutes after 18 h local time (Table 1). The second TSX image was acquired on 2018-01-11, one day before the second S1 image (2018-01-12). On the day in between, the avalanche activity was very low (Fig. 2) and meteorological conditions were relatively stable (SLF, 2018b).

To assess avalanche detection of entire Switzerland, S1 acquisitions were carefully selected from multiple orbits during a 5 day period from before and after the first event (Gray shading in Fig. 2, acquisition details in Table A1).

To analyze the second avalanche event, the SLF ordered optical SPOT-6 images acquired with the single-pass multi-strip collection mode. With this mode the most of the Swiss alps ($300\times40\,\mathrm{km}^2$) could be imaged in a single day (2018-01-24), at a resolution of 1.5 m. These images were visually searched for avalanches by an expert (Bühler et al., 2019). For comparison we also analyzed TSX data from 2018-02-02, acquired 9 days later.

3 Radar backscatter physics of avalanches

We detected avalanches based on the radar backscatter signal and their visual appearance (shape). Fig. 3 illustrates a classification scheme from (International Commission of Snow and Ice, 1981). The scheme suggests that all avalanche types are composed of three different zones but for some avalanche types (e.g. loose snow avalanches) zones can be difficult to differentiate. The most upslope part is the release area (Fig. 3, blue) with a smooth surface caused by the failure of the weak layer, followed by the zone of transition (purple) with the stauchwall and some deposition caused by the terrain roughness, and finally the tongue-shaped zone of deposition (red) at the bottom which is covered by densely compacted snow granules.

Based on snow properties, the different zones show a different radar backscatter signal. In first order scattering physics the total backscatter intensity of a snow pack, σ^0_{snow}, can be composed of scattering from the snow surface, σ^0_{surf}, scattering from the snow volume, σ^0_{vol}, scattering from the ground below the snow pack, $\sigma^0_{\mathrm{ground}}$, and scattering from higher order interactions between different structures in the snow pack $\sigma^0_{\mathrm{inter}}$. Currently, there exists no specific model tailored to the backscatter properties of snow avalanches (cf. Eckerstorfer and Malnes, 2015, Sect. 5.3), however, general scattering physics from bi-continuous media and rough surfaces can be applied. In that sense, scattering in snow increases with the spatial correlation length of ice

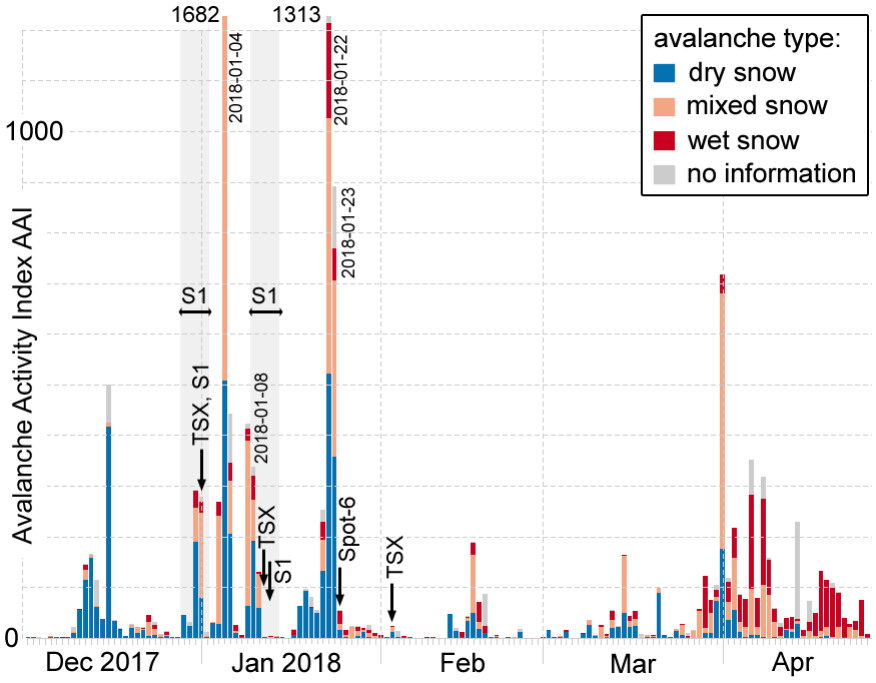

Figure 2. The avalanche activity index is the weighted sum of all reported avalanches for Switzerland (Schweizer et al., 2003, 1998). Dry snow avalanches which started high up but were slowed down at medium altitude by wet snow are indicated as "mixed snow" in the legend. Satellite acquisitions dates are indicated by arrows. Images for the multiorbital S1 composite were acquired during the gray shaded periods (see also Table A1). Figure modified after Winkler et al. (2019).

grains (Wiesmann et al., 1998) and also with increased surface- and interface roughness and with decreasing incidence angle θ (Leader, 1971; Fung and Eom, 1982; Kendra et al., 1998).

$$\sigma^0_{\text{snow}}(\theta) = \sigma^0_{\text{surf}}(\theta) + \sigma^0_{\text{vol}}(\theta) + \sigma^0_{\text{ground}}(\theta) + \sigma^0_{\text{inter.}}(\theta) \tag{1}$$

For plain dry snow of few meters depth scattering at the ground usually dominates the signal because microwaves between 1 and 10 GHz are weakly scattered at the snow surface and within the snow volume and penetrate therefore the snow pack to the ground (Xu et al., 2012; Cumming, 1952; Rignot et al., 2001), see also conclusion and simulations in Leinss et al. (2015). For dry snow the ground roughness determines the backscatter signal but for smooth ground mainly forward scattering (away from the sensor) occurs. For deeper snow or higher frequencies the signal can be dominated by volume scattering (Watte and MacDonald, 1970).

In contrast to plain dry snow, snow is deeper and denser in the deposition zone where the surfaces of the avalanche debris can be very rough. Because of the higher dielectric contrast due to the higher permittivity (Matzler, 1996), the contribution of

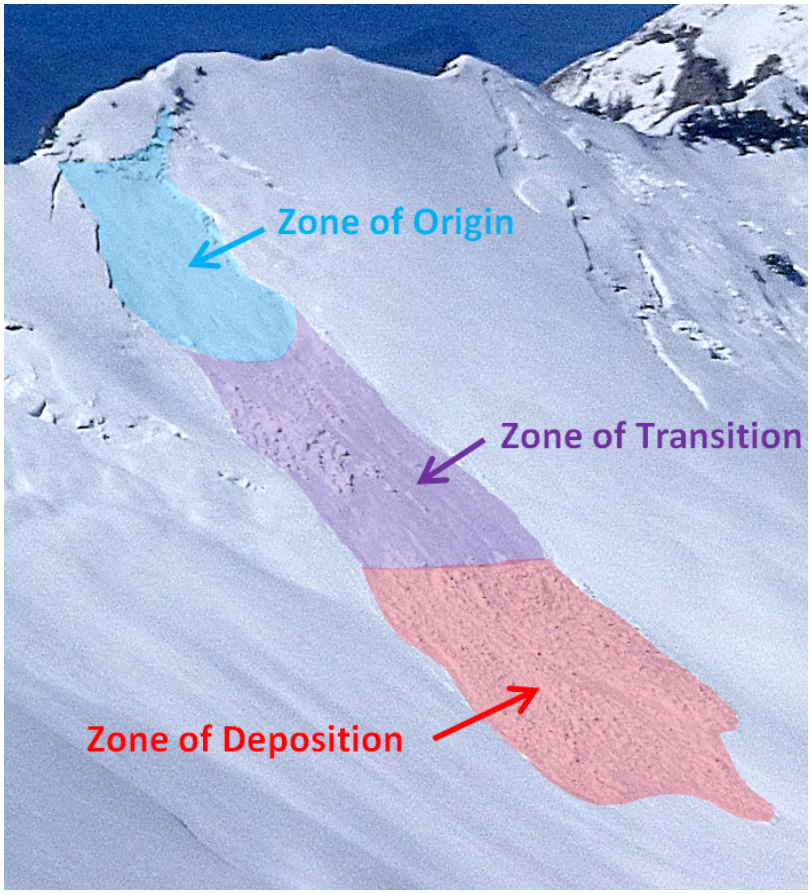

Figure 3. Different avalanche zones illustrated by a slab avalanche.

σ^0_{vol} and σ^0_{surf} to the total backscatter intensity increases. Both the rough surface and the debris volume scatter radiation more omnidirectional (diffuse scattering) compared to an undisturbed snow pack over smooth ground (specular scattering).

For plain wet snow, however, the incoming radar waves are weakly backscattered at the air-snow interface because most radiation is lost by absorption (Tiuri et al., 1984; Cumming, 1952) and also by forward scattering described by Fresnel coefficients.

As the volume and ground contribution is negligible for wet snow avalanche debris, the dominant backscatter signal results from omnidirectional scattering at the increased surface roughness in the deposition zone of avalanches (cf. Eckerstorfer and Malnes, 2015, Sect. 5.3).

Based on the above scattering physics, the zone of origin is very difficult to detect in radar images because the weakly scattering snow volume is reduced without major changes in the surface roughness. The zone of transition should be only sometimes visible, depending on the deposition of avalanche debris. Therefore, mostly the deposition zone can be detected by a brighter backscatter signal and the mostly elongated, tongue shaped geometry.

To obtain a high backscatter contrast with respect to the avalanche surrounding the local incidence angle θ should be far away from zero (i.e. away from layover) to avoid the intense specular backreflection from smooth surfaces. Therefore, the visibility of avalanches in radar images should be much better for slopes facing off the radar. These slopes are also imaged with a higher ground-range resolution $\delta_{\mathrm{sr}}/\cos\theta$ which can be close to the slant-range resolution δ_{sr}.

4 Methods

4.1 Data preprocessing

All radar products were downloaded in the single look complex (SLC) format. The data were preprocessed with the ESA SNAP Sentinel-1 toolbox and also with the GAMMA software for comparison. The workflow using GAMMA was implemented with Nextflow (Di Tommaso et al., 2017) to speed up execution and code development and to ensure a reproducible analysis. Preprocessing consists of coregistration, multilooking for reduction of radar speckle (TSX: 6×5 px, S1: 4×1 px), orthorectification, and generation of radar shadow and layover masks. The SNAP workflow for S1 images is shown in Fig. A1. We did not apply any radiometric terrain correction as the visible topography helps to identify the avalanche path direction.

For orthorectification we used the Swiss elevation model SwissAlti3D (2013) downsampled from 2 m to 30 m resolution. We noticed, however, that despite of using the same DEM and output resolution, sharp topographic features seem to be better orthorectified with the GAMMA software which might use a more precise spatial interpolation. The radar images were orthorectified to a resolution of 5x5 m (TSX) and 15x15 m (S1) and the backscatter signal in dB was saved to geotiff files. The exact radiometric normalization is irrelevant, because we did not apply any radiometric terrain correction (Small, 2011) and different ellipsoidal corrections ($\sigma^0_{\mathrm{E}}, \gamma^0_{\mathrm{E}}$) differ only by almost constant factors. Since the TSX data was acquired with a single polarization (the co-polar channel HH) we also used only the co-polar channel (VV) of the two available polarizations of S1 to obtain a fair comparison. For the multiorbital composites, we used both polarizations of S1 (VV, VH).

4.2 Two-image composite avalanche detection

Although avalanches could be manually detected in single radar images they are difficult to analyze with automatic methods. As radar systems carry their own illumination system the backscatter signal is primarily determined by topography and land cover type. It is therefore common practise to analyze change detection images to separate sudden backscatter changes from stable topographic and land cover features (Wiesmann et al., 2001; Eckerstorfer and Malnes, 2015). To correct for large-scale backscatter changes due to wet snow a 500 m highpass filter was applied to the backscatter difference between two consecutive images. Examples for TSX and S1 are shown in Figs. 4a and 4b. To create the images, the backscatter intensities in dB were normalized by clipping the lower and upper 1%. Consecutive images were then stored in the channels [R, G, B] = [img2, img1, img1] so that backscatter changes are well visible by the red-cyan contrast. From the images (TSX and S1) avalanche outlines were drawn manually.

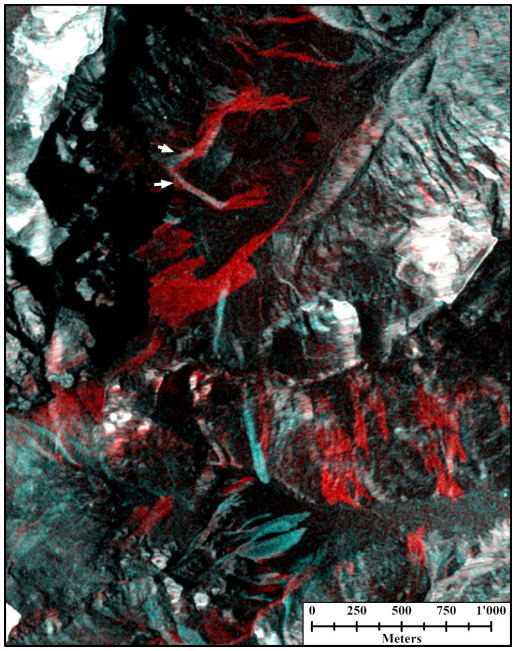

(a) Subset of change detection image tsx(12-31 / 01-11).

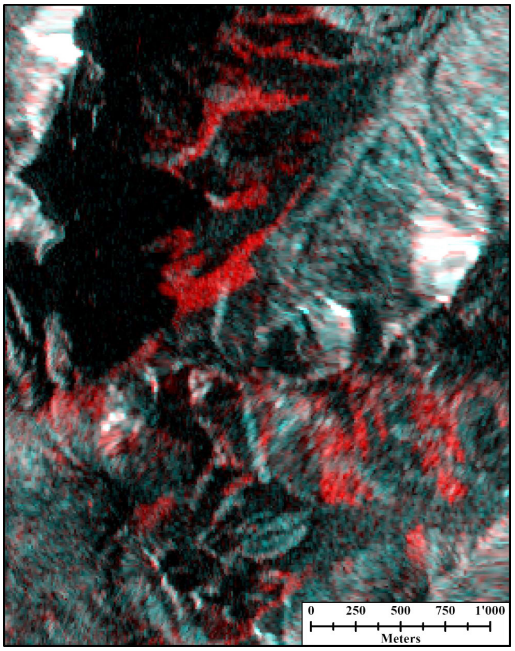

(b) Subset of change detection image S1(12-31 / 01-12).

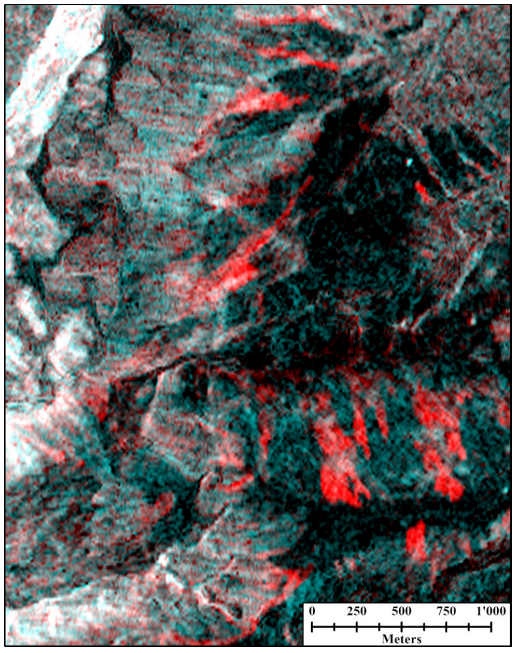

(c) Subset of S1 multiorbital change detection image from the two data sets 2017-12-28 – 2018-01-01 vs. 2018-01-09 – 2018-01-12.

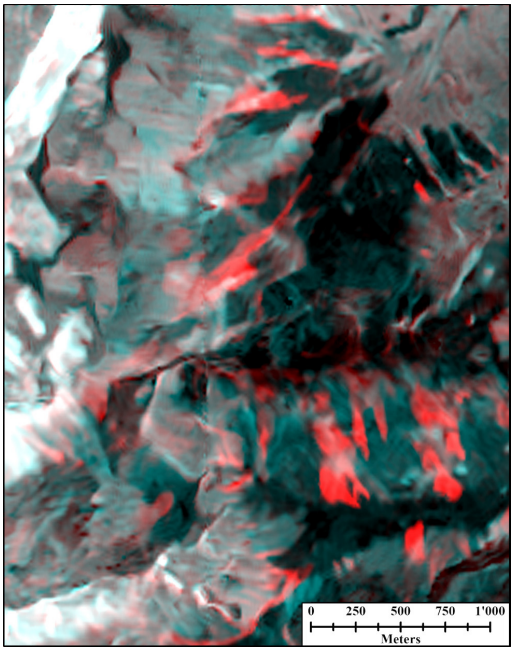

(d) Multiorbital S1 change detection image as in (c) but with non-local mean filter applied.

Figure 4. (a,b) TSX and S1 change detection images of a subsets of the study area (cf. Fig. 1). The radar view direction is ascending (left to right) incidence angles are 29°and 34°. Arrows in (a) indicate old avalanches overrun by new ones. (c) S1 multiorbital composite with (d) non-local mean filter applied. All TerraSAR-X and Copernicus Sentinel data (2019) were orthorectified with the swissALTI3D © 2019 swisstopo (JD100042), reproduced with the authorisation of swisstopo (JA100120).

The change detection images allow for a temporal classification of avalanches into three classes (*new, old, unsure*). *New* avalanches appear red because of increased backscattering and are therefore assumed to have occurred between the first and the second acquisition. *Old* avalanches, with a decreasing backscatter signal, appear blue are therefore assumed to have occurred before the first acquisition. Bright features with unchanged backscatter intensity appear almost white and are classified as *unsure* if they look like avalanches.

4.3 Multiorbital composite image for Switzerland

The free and systematic availability of S1 radar images and the short revisit period of six days allow for creation of an RGB composite change detection image covering entire Switzerland. Therefore, 12 images, acquired between 2017-12-28 and 2018-01-01 from different orbits, were combined into an image before the first avalanche event (Jan 4$^{\text{th}}$). Another 12 images, acquired between 2018-01-09 and 2018-01-12 with an identical imaging geometry, were used for the post-avalanche event image. The images (listed in Table A1) were preprocessed according to Sect. 4.1. To reduce radar speckle we averaged both polarizations and weighted the cross-pol channel (VH) by the ratio a of the co- and cross-pol backscatter intensities averaged over the acquisition footprint:

$$S = \frac{S_{\text{VV}} + a\, S_{\text{VH}}}{1 + a} \qquad \text{with} \qquad a = \frac{\langle S_{\text{VV}} \rangle}{\langle S_{\text{VH}} \rangle} \tag{2}$$

Then, the weighted mean was converted to dB and scenes from different ascending and descending orbits were averaged. Thereby, a relatively homogeneous bright image is generated where layover areas lighten up the relatively dark slopes facing away from the radar without screening too much of the contained details (Fig. 4c). To further reduce noise but to preserve edges in the mosaic images, we applied a non-local mean filter (Jin et al., 2011; Condat, 2010). The filtered image is shown in Fig. 4d.

4.4 Relative brightness of snow avalanches

To analyze the brightness of avalanches relative to their surrounding, we calculated the ratio of the mean backscatter signal of an avalanche area and its surrounding area. Therefore, a manually generated avalanche mask was dilated once by 9 and once by 18 pixels. The difference of the two masks defines the surrounding. For the avalanche mask, the visual avalanche mask was eroded by 3 pixels to reduce manual contouring errors. To obtain statistically significant results we calculated the backscatter ratios only for avalanches and surrounding areas larger than 100 pixels.

4.5 Automated avalanche detection

As manual avalanche mapping is time consuming, a reliable automation of this process would make the mapping data quickly available for further application. Therefore, different attempts have been made to automatically detect avalanches mainly on the two satellite platforms S1 (Vickers et al., 2016; Wesselink et al., 2017; Abermann et al., 2019; Eckerstorfer et al., 2019), and Radarsat-2 (Hamar et al., 2016; Wesselink et al., 2017). The general workflow in these papers is quite similar to ours.

All methods are based on two-image change detection, application of various masks (layover, shadow, water bodies, forest), thresholding and filtering of extracted avalanche properties.

In addition to a shadow and layover mask, we applied a slope dependent mask to limit the detection to potential avalanche deposition zones for which we expect the strongest backscatter change. By definition, friction is larger in the deposition zone than the downhill-slope force. Therefore, slopes with an inclination larger than 35°, which typically occur in the zone of origin, are masked out (Bühler et al., 2009).

For noise reduction but to preserve avalanche edges, a 5×5 px median filter was applied to the backscatter difference images in dB. As avalanches should have a well defined edge, an edge mask was generated by applying a Sobel filter with a 5×5 kernel to the median filtered difference image.

In the median filtered difference image, from all pixels brighter than a threshold of 4 dB, the brightest 5% were considered as the mask of potential avalanches. The threshold was determined empirically based on TSX data but other authors also used thresholds of 4–6 dB (Eckerstorfer et al., 2019; Karbou et al., 2018; Vickers et al., 2016). To remove isolated bright pixels from the mask, we determined around each continuous area an ellipse and removed areas with a major axis shorter than 15 pixels (TSX: 45 m, S1:225 m). Additionally, only potential avalanches for which more than 10 pixels intersect with the edge mask were considered for the final avalanche mask.

4.6 Comparison between mapping results

None of the mapping results obtained from TSX, S1, or SPOT-6 can be considered as real ground truth and different avalanches or avalanche shapes were detected with the different methods and satellites. Also, ambiguous relations can exist when a single large avalanche in one mapping result appears as multiple smaller avalanches in another mapping result. This makes the evaluation of binary classifies (e.g. probability of detection or false discovery rate) difficult or even impossible. We refrained from using a pixel-to-pixel comparison which would have demanded a manual mapping precision on the pixel level which contradicts the subjective mapping by an experienced expert who sometimes estimates an avalanche outline from discontinuous avalanche patches.

As a remedy we compare results from two data sets A and B by reciprocal counting of avalanches which overlap in both data sets (considered as "found") and avalanches which do not overlap (considered as "not found"). These numbers differ depending on the direction in which the comparison is done (A→B or B→A). Depending which data sets is considered as ground truth, avalanches which were "not found" can be either regarded as false negative alarms (missed) or as false positive alarms (false alarm).

For conciseness we abbreviate the RGB change detection images by acquisition month and day (mm-dd / mm-dd).

Table 2. Number and classification of manually detected avalanches in TSX images covering the first and the second avalanche period.

change detection image	total	*new*	*unsure*	*old*
tsx(12-31 / 01-11)	267	164	84	19
tsx(01-11 / 02-02)	351	170	146	35

5 Results

5.1 TSX change detection

In the change detection image tsx(12-31 / 01-11), covering the first avalanche period, a total of 267 avalanches were manually detected in the study area (red polygon in Fig. 1). As detailed in Table 2, 164 avalanches were classified as *new* and 19 were classified as *old* avalanches. For 84 avalanches a clear assignment to *new* or *old* was not possible. Therefore, we assigned them to the class *unsure*. For example, in the upper part of Fig. 4a arrows indicate two large new avalanches which completely covered two small old avalanches. Therefore, their backscatter signal did not change and these old avalanches were classified as *unsure* (though they could be classified as *old* using spatial context information).

In the change detection image tsx(01-11 / 02-02), covering the second avalanche period, a total of 351 avalanches were detected, composed of 170 *new* avalanches, 35 *old* ones and 146 *unsure* cases. Most of these *unsure* avalanches were actually classified as *new* after the first avalanche period but overrun by new avalanches during the second avalanche period (compare Fig. A2 with Fig. A3). Therefore, the number of *old* avalanches seems to remains low.

5.2 TSX compared to optical SPOT-6

The SPOT-6 images were acquired immediately after the second avalanche event in the morning of Jan 24th. Avalanche were mapped by E. Hafner in SPOT-6 images (Bühler et al., 2019). They found that only 24% of outlines were clearly visible; 76% of the avalanches outlines were estimated between partially visible release and deposit areas. In the study area, the SPOT-6 avalanches did not contain any age information but the authors conclude that $20 - 45\%$ of avalanches were already released many of them are actually old avalanches.

Due to the 11 day revisit time of TSX, the next available TSX image was acquired 9 days after the second event in the evening of Feb 2nd. During this 9 days surface melt occurred followed by about 20 cm of new snow on Feb 1st. Due to changing snow properties the contrast between avalanches and the surrounding snow has very likely decreased. Without knowledge of the SPOT-6 mapping results, avalanche were mapped in the TSX images independently by the second author of this work. The outlines differed significantly, however, most likely because different features (avalanche origin, path, deposit zone) are visible in optical and radar images. Therefore we decided for a feature-based comparison, i.e. overlapping polygon are considered as detected in both data sets. Avalanches split up into discontinuous polygons were counted separately, even if all polygons overlap with one single large polygon in the other data set (Sect. 4.6).

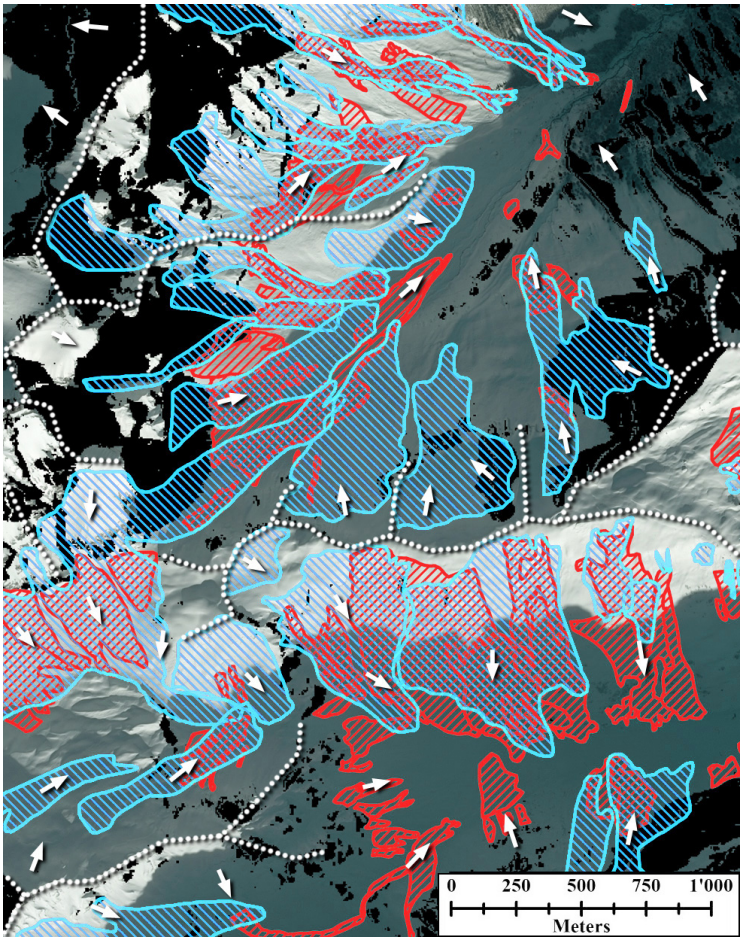

Figure 5. Manually mapped avalanches (blue) from the SPOT-6 image 2018-01-24 (background) vs. change detection results from tsx(01-11 / 02-02) (red, all classes) in a subset of the entire study area (cf. Fig. 1). Orthorectified with the swissALTI3D © 2019 swisstopo (JD100042), reproduced with the authorisation of swisstopo (JA100120). Radar shadow is added in black. Dots show mountain ridges and arrows the down-slope direction.

Table 3. (a) Number of avalanches in TSX change detection image compared to avalanches which were also detected in the optical SPOT-6 data. (b): reverse correspondence of avalanches from SPOT-6 to *new* and *unsure* avalanches from the radar change detection image. Avalanches which were not found are grouped depending on if they are located in the cast shadow (a) or in the radar shadow (b).

(a) of *new/unsure* in tsx(01-11 / 02-02) → SPOT-6 (01-24)

total	found	not found (in / not in cast shadow)	
316	215	101	(84 / 17)

(b) of SPOT-6 (01-24) → *new/unsure* in tsx(01-11 / 02-02)

total	found	not found (in / not in radar shadow)	
286	125	161	(57 / 104)

Despite of non-optimal acquisition timing and mapping conditions, Table 3a shows for the change detection image tsx(01-11 / 02-02) that 68% (215/316) of the avalanches detected as *new* or *unsure* were also detected in the SPOT-6 image. Interestingly, of the remaining third (101/316) the majority (84 avalanches) were located in the cast shadow.

Vice versa, 44% (125/286) of the optically detected avalanches were also found in the TSX change detection image (Table 3b) but more than half of the optically detected avalanches were not found. 20% (57/286) could not be found because they are located in the radar shadow and 36% (104/286) had a too low backscatter contrast to be visible with radar. We did not found significant differences in area for the lower detection limits: for both, TSX and SPOT-6 the smallest detectable avalanches had an area of 500 m^2 (Sect. 5.6).

Using the temporal information from radar change detection the 125 avalanches detected with SPOT-6 but also with TSX (Table 3b) can be further classified into 27 *new*, 38 *unsure*, and 6 *old* avalanches. The remaining 54 avalanches could not be unambiguously classified, because they cover areas differentiated into multiple different classes by radar whereas such a temporal classification is difficult with single SPOT6 images (Bühler et al., 2019).

Figure 5 shows a subset of the SPOT-6 images and visualizes the manually mapped avalanches. Especially in the lower part of the image, in the cast shadow, many small radar-detected avalanches (red) were not found in the optical analysis (blue). With radar, avalanches could generally not be detected in the radar shadow or layover (added with black) but also many other avalanche were missed by radar.

5.3 TSX compared to S1 change detection

To asses the added value of high resolution TSX images we compared them to medium resolution S1 images. We chose the first avalanche period to simplify counting because of less overlapping old and new avalanches. In the S1 change detection image S1(12-31 / 01-12) a total of 89 *new*, 13 *unsure*, and 16 *old* avalanches were found. The S1 image shows a significantly lower resolution than TSX (Fig. 4a vs. Fig. 4b) such that small avalanches (yellow in Fig. 6) are more likely to be missed.

As detailed in Table 4, from the 89 *new* avalanches, 83 were also found by TSX. They correspond to 76 *new* and 7 *unsure* avalanches; 6 avalanches were not found. Vice versa, two thirds (104/164) of the avalanches found in tsx(12-31 / 01-11) corre-

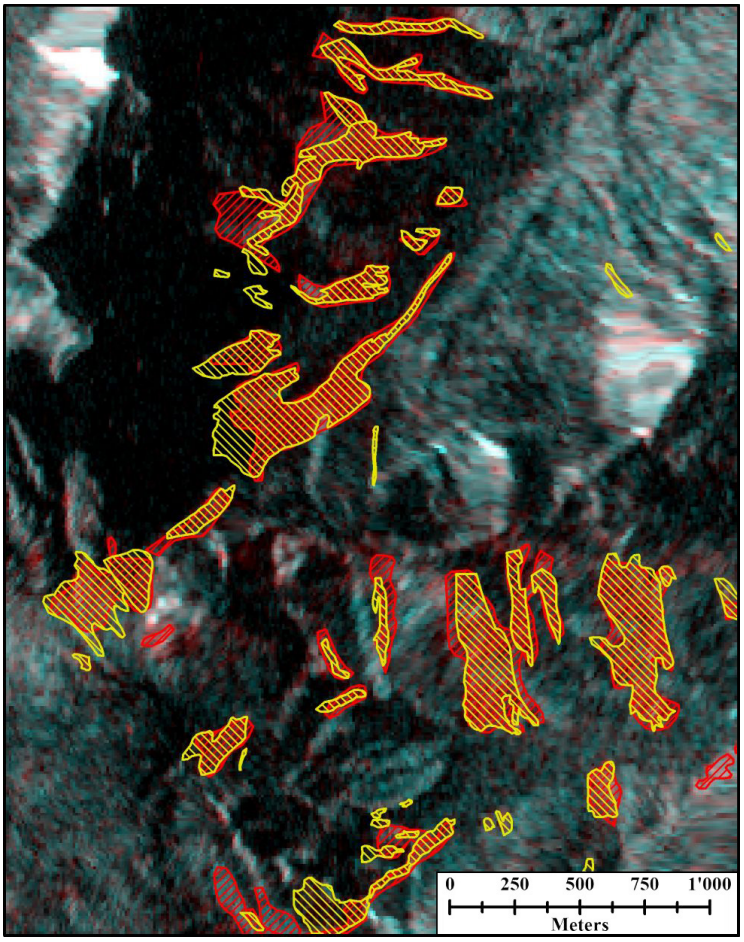

Figure 6. Manually mapped *new* avalanches (in red) from the change detection image S1(12-31 / 01-12) compared to manually mapped *new* avalanches from tsx(12-31 / 01-11) (yellow). No mask is shown for avalanches classified as *old* or *unsure*. The images from which the masks were derived are shown in Figs. 4a and 4b. Image orthorectified with swissALTI3D © 2019 swisstopo (JD100042), reproduced with the authorisation of swisstopo (JA100120).

spond to the 83 avalanches also found with S1. One third (60/164) was not found, mostly because they were too small to be detected with S1. We found that the smallest avalanches detected by S1 have an area of around 2000 m^2 (Sect. 5.6).

Table 4. (a) Number of manually detected *new* avalanches in S1(12-31 / 01-12) which were also detected as *new* or *unsure* in the change detection image tsx(12-31 / 01-11). (b) reverse correspondence.

(a)	of *new* in S1(12-31 / 01-12)	→	tsx(12-31 / 01-11)
	total	found (*new / unsure*)	not found
	89	83 (76 / 7)	6

(b)	of *new* in tsx(12-31 / 01-11)	→	S1(12-31 / 01-12)
	total	found (*new / unsure*)	not found
	164	104 (100 / 4)	60

5.4 Multiorbital S1 change detection composite

By combining S1 acquisitions from multiple ascending and descending orbits, we minimized areas affected by radar layover (areas with radar shadow appear in layover when imaged with the opposite pass direction). The multiorbital change detection composite is shown in Fig. 7 and covers entire Switzerland during the first avalanche period. In the full, non-local mean filtered 15 m-resolution image, which is available online (Leinss et al., 2019), we manually counted 7361 avalanches but did not draw any polygons. We found that avalanches reaching below the wet snow line were much better visible than avalanches from the dry snow zone. The subset shown in Fig. 4c illustrates the mitigation of layover (in the upper and lower right), the speckle reduction and the enhanced resolution compared to the single orbit S1 image in Fig. 4b. Only areas near radar shadow loose contrast and show a reduced avalanche visibility because the added layover image does not contain useful information.

The comparison of the multiorbital S1 mapping results with the high resolution TSX data is detailed in Table 5. In the study area a total of 136 *new* avalanches were manually detected in the multiorbital image (S1-MO). Of these, 104 avalanches match with avalanches detected in the corresponding single orbit TSX change detection scene (95 of them with *new* avalanches, 9 with *unsure*), whereas 32 avalanches were not found with TSX. 17 of the 32 avalanches could not be detected because they are in the shadow/layover areas of TSX. Vice versa, 110 of 164 TSX avalanches were also detected in the multiorbital S1 composite whereas 54 TSX avalanches were not detected.

5.5 Automated avalanche detection

For the implemented automatic avalanche detection algorithm we chose a threshold of 4 dB for the relative brightness of avalanches which corresponds to the upper 82% of the avalanche brightness distribution shown in Fig. 8a. The figure is based on 99 of 164 *new* avalanches which cover more than 100 pixels (Sect. 4.4) and which were selected from tsx(12-31 / 01-11) for the entire study area (red rectangle, Fig. 1). The threshold to mask out areas steeper than 35° (Sect. 4.5) is supported by the slope-dependent distribution of avalanche pixels in Fig. 8b. With these settings, the automatic methods identified about two

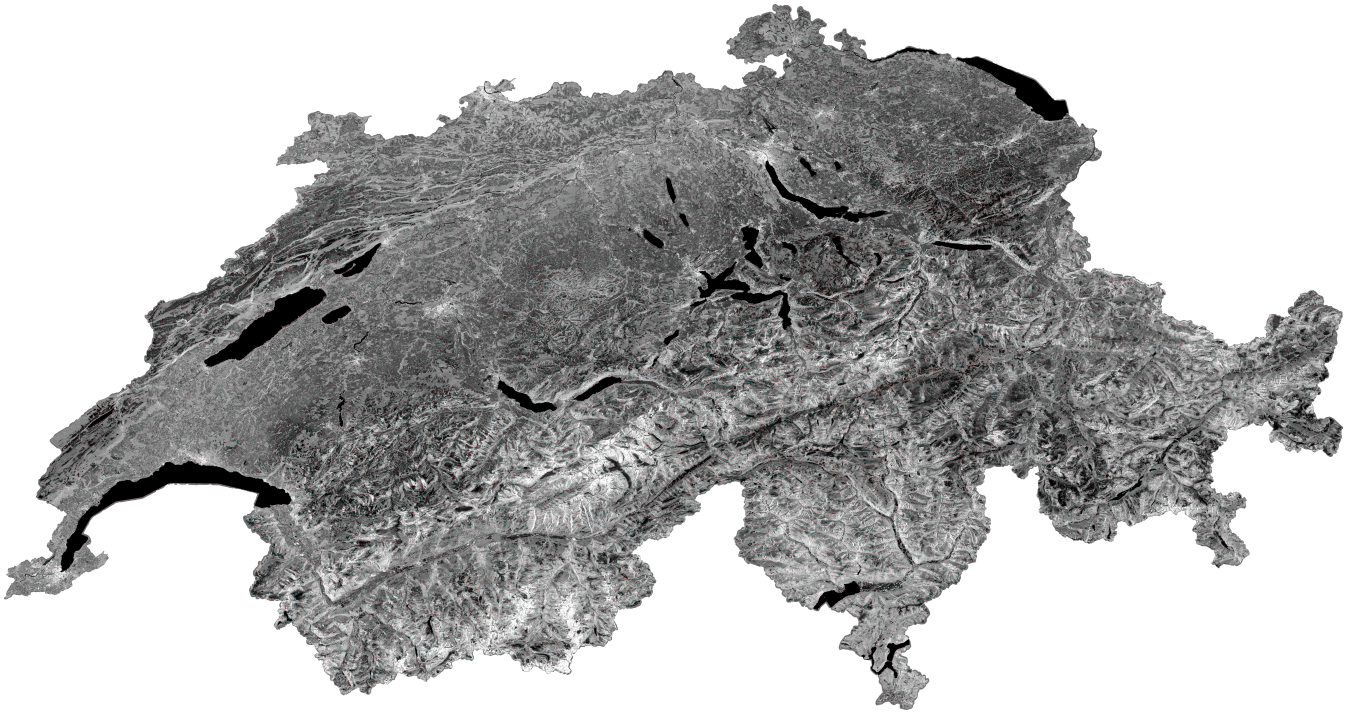

Figure 7. In the 15 m-resolution multiorbital S1 change detection mosaic, covering entire Switzerland for the first avalanche period around Jan 4th, we manually counted 7361 *new* avalanches. When zooming into the image, many avalanches are visible in red. The image is combined from each 12 acquisitions from 2017-12-28 until 2018-01-01 and from 2018-01-09 until 2018-01-12 and is available online (Leinss et al., 2019). All Copernicus Sentinel scenes (2019) were orthorectified with the swissALTI3D © 2019 swisstopo (JD100042), reproduced with the authorisation of swisstopo (JA100120).

Table 5. (a) Number of the *new* avalanches in the S1 multiorbital change detection image (S1-MO) compared to avalanches in the TSX change detection image. Reverse correspondence in (b).

(a) *new* in S1-MO(12-28+4d / 01-09+4d) →tsx(12-31 / 01-11)

total	found (*new/unsure*)		not found (in/not in shadow)	
136	104	(95 / 9)	32	(17 / 15)

(b) *new* in tsx(12-31 / 01-11) →S1-MO(12-28+4d / 01-09+4d)

total	found	not found
164	110	54

thirds of the manually identified avalanches in the same image pair. Here we considered the manually determined avalanche mask as a proxy for the true extend of the deposition zone. We are aware that the significance of such a comparison is limited.

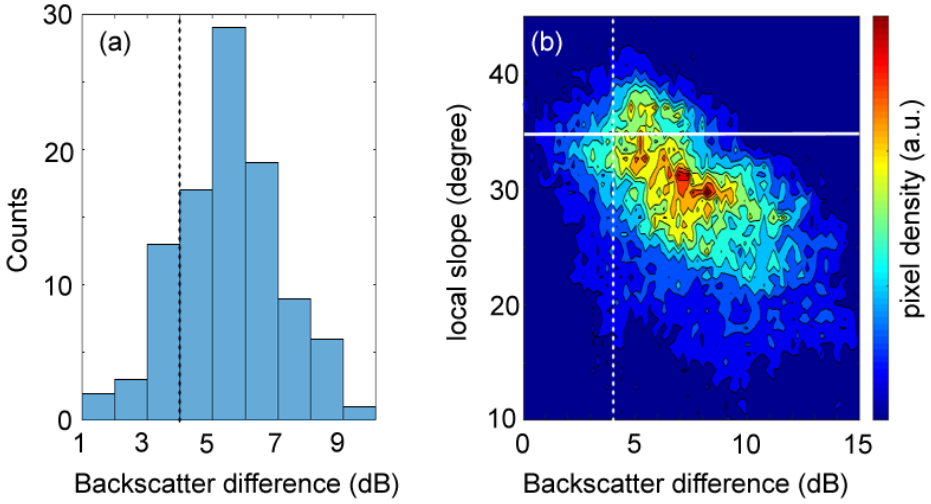

Figure 8. (a) Histogram of the mean relative brightness of avalanches compared to surrounding area for manually mapped *new* avalanches of tsx(12-31 / 01-11) in the study area (red polygon, Fig. 1). (b): Relative brightness of the avalanche pixels in relation to the local slope angle. Lines indicate the thresholds for the backscatter difference (dashed) and the slope-dependent mask (solid).

Nevertheless, the advantage of this comparison is that the performance of the detection algorithm is directly compared to the results of a human avalanche mapping expert.

For the first image pair tsx(12-31 / 01-11) Table 6a details that 110 of 164 manually mapped *new* avalanches were also found with the automated detection whereas 54 were not found. As shown in Fig. 9, these "missed" avalanches are often small avalanches which were filtered out by the algorithm. Vice versa, of 138 automatically detected avalanches 21 were not found manually (Table 6b).

When considering the total number (164) of manually detected avalanches in the study area (red polygons in Fig. 1) as truth one can assign avalanches which were also found automatically to *true positive* (TP = 110), i.e. correctly detected. The remaining avalanches, which were not automatically detected, are then assigned to *false negative* (FN = 54), i.e. incorrectly rejected. With this assumption the probability of detection (POD) and the miss rate or false negative rate (FNR) can be calculated:

$$\mathrm{POD} = \frac{\mathrm{TP}}{\mathrm{TP} + \mathrm{FN}} \qquad \text{and} \qquad \mathrm{FNR} = \frac{\mathrm{FN}}{\mathrm{TP} + \mathrm{FN}} = 1 - \mathrm{POD} \tag{3}$$

Further, one can assign automatically detected avalanches which were not manually found to *false positive*s (FP = 21), i.e. incorrectly detected. When assuming that the number of correctly detected avalanches is given by TP = 110, the false discovery rate (FDR) reads

$$\mathrm{FDR} = \frac{\mathrm{FP}}{\mathrm{FP} + \mathrm{TP}} \tag{4}$$

With that one obtains a POD = 67 %, a miss rate FNR = 33 % and a false discovery rate FDR = 16 % for tsx(12-31 / 01-11).

For the second image pair tsx(01-11 / 02-02) only 82 of 170 manually detected *new* avalanches were automatically found whereas 88 were not found (Table 6c). Vice versa, 54/179 automatically detected avalanches were not found manually (Ta-

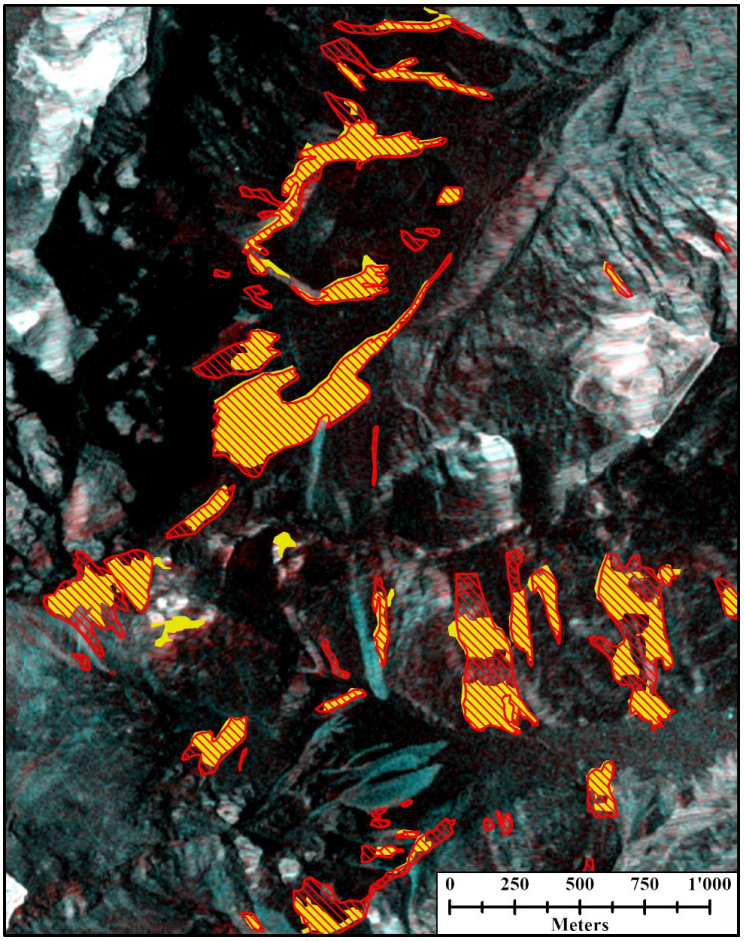

Figure 9. Comparison between detected *new* avalanches when manually mapped (red) and automatically detected (yellow) in the TSX acquisition pair 2017-12-31 vs. 2018-01-11. The TSX background image is shown without mask in Fig. 4a. Orthorectified with the swissALTI3D © 2019 swisstopo (JD100042), reproduced with the authorisation of swisstopo (JA100120).

Table 6. Number of automatically detected *new* avalanches compared to the number of manually detected *new* avalanches.

(a) man:tsx(12-31 / 01-11) → auto:tsx(12-31 / 01-11)

total	found	POD	not found	FNR
164	110	67%	54	33%

(b) auto:tsx(12-31 / 01-11) → man:tsx(12-31 / 01-11)

total	found	not found	FDR
138	117	21	16%

(c) man:tsx(01-11 / 02-02) → auto:tsx(01-11 / 02-02)

total	found	POD	not found	FNR
170	82	48%	88	52%

(d) auto:tsx(01-11 / 02-02) → man:tsx(01-11 / 02-02)

total	found	not found	FDR
179	125	54	40%

(e) man:S1(12-31 / 01-12) → auto:S1(12-31 / 01-12)

total	found	POD	not found	FNR
89	68	76%	21	24%

(f) auto:S1(12-31 / 01-12) → man:S1(12-31 / 01-12)

total	found	not found	FDR
92	72	20	23%

ble 6d). Assuming again that the manually detected avalanches are the true avalanches one obtains a POD of 48 %, a FNR of 52 %, and a FDR = 40 %. The results are expected to be worse compared to the first period, because mapping of *new* avalanches was very difficult for the second period where many old and new avalanches overlapped such that many *unsure* cases occurred for which the backscatter signal changed less than the threshold of 4 dB.

The automated algorithm was also run on the S1 images pair S1(12-31 / 01-12). As detailed in Table 6e, 68 of 89 manually detected *new* avalanches were also found automatically whereas 21 were not found. Vice versa, of 92 automatically mapped avalanches 72 were also found manually and 20 were not found (Table 6f), resulting in a POD = 76%, a FNR = 24%, and a FDR = 23%.

The higher POD and lower FNR for S1 compared to TSX indicates only, that with S1 the automatic method can detect a larger fraction of the manually detected avalanches. It does not indicate that results obtained from S1 are better compared to TSX data where in total more avalanches were detected.

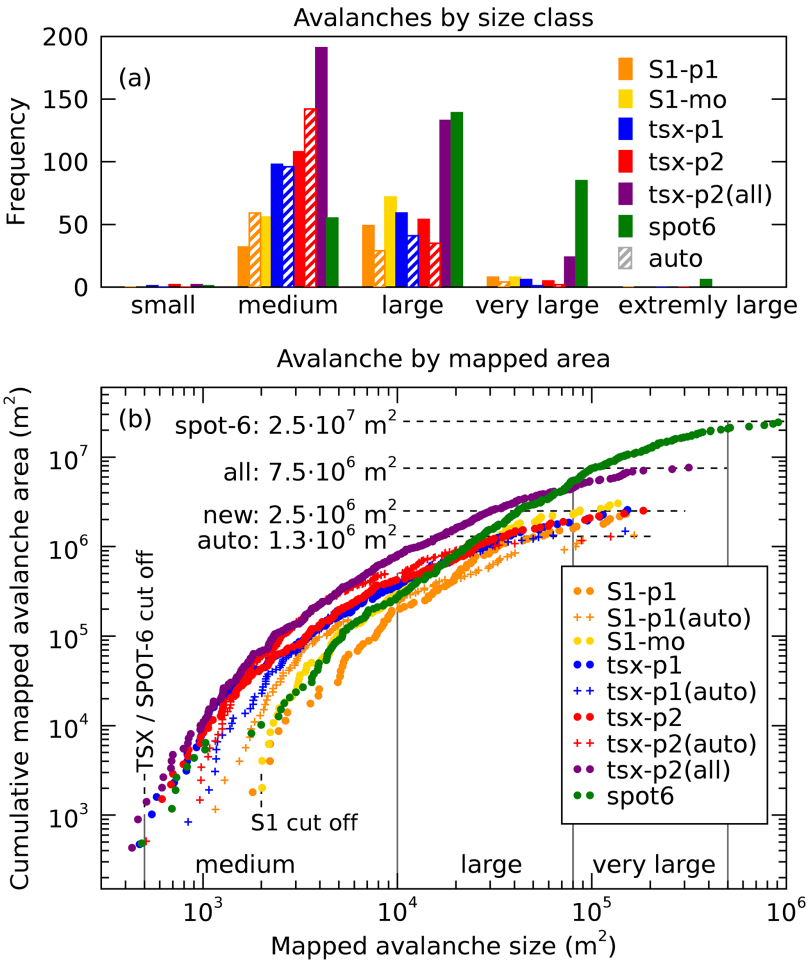

Figure 10. (a): Classification of mapped avalanche area into size classes. (b): the cumulative avalanche area $\Sigma_1^i A_i$ plotted over avalanche size (A_i) reveals that the smallest avalanches size detected by TSX and SPOT-6 is about 500 m^2, 2000 m^2 for S1, and around 1000 m^2 for the automatic methods. The total cumulative areas differ by an order of magnitude: with radar only bright deposit areas of *new* avalanches were mapped automatically ($1.3 \cdot 10^6$ m^2), and less-bright areas were added manually ($2.5 \cdot 10^6$ m^2). Summing all classes (*new, old, unsure*) in TSX images results in $7.5 \cdot 10^6$ m^2 which is one third of the cumulative area of SPOT-6 outlines ($2.5 \cdot 10^7$ m^2) which cover also older avalanches and for which outlines of the entire avalanche area (release, path, deposit) were either clearly visible or were at least estimated.

5.6 Size distribution of detected avalanches

The size distribution of detected avalanches depends on sensor resolution and also on which features are actually visible by the sensor. For radar sensors it is likely that only the deposit area is mapped, whereas for the SPOT-6 dataset care was taken to map (or at least estimate) the entire avalanche area, including the release area (Sect. 5.2). Because with radar only partial areas were mapped, simple size distributions (Fig. 10a) may appear shifted. To provide more detailed insight we plotted the cumulative area $\Sigma_1^i A_i$ of all avalanches sorted by their apparent area A_i (Fig. 10b).

The smallest detectable avalanche size can be found in the lower tail of the curves in Fig. 10b: for TSX and SPOT-6 the smallest avalanches have about 500 m^2, 2000 m^2 for S1, and around 1000 m^2 for the automatic methods.

It may surprise that in the study region the total avalanche area in SPOT-6 images is an order of magnitude larger ($2.5{\cdot}10^7$ m^2, green curve in Fig. 10b) than the total area of manually radar-detected *new* avalanches from TSX and S1 (red, blue, and orange dots: $2.5{\cdot}10^6$ m^2). A factor of three remains when comparing the area of all (*new, old*, and *unsure*) avalanches detected by TSX (purple in Fig. 10b) with SPOT-6 which does not contain any age classification. Considering the fact that with radar mainly the deposition zone can be mapped a difference of a factor of three is reasonable.

6 Discussion

6.1 Radar change detection images

The temporal information from radar change detection makes it possible to differentiate relatively clearly between new and old avalanches, at least for low avalanche activity where old avalanches are rarely overrun by new ones. This can be seen as a major advantage compared to optical images for which temporally dense time series are not reliably available due to weather conditions. The missing temporal information can lead to an overestimation of the avalanche area and (Bühler et al., 2019) report that deposit areas of large avalanches ($> 10\,000\,\mathrm{m}^2$) remain visible for several weeks.

Nevertheless, for strong avalanche activity, the differentiation of overlapping avalanches is difficult even with radar. For example, we found a large number of *unsure* avalanches for the second analyzed avalanche event (Sect. 5.1) which could be assigned to *new* avalanches of the first event. For temporal separation, fast repeat times of current radar satellites, like 6 days when combining the two S1 satellites is a major advantage compared to other satellites (TSX: 11 days, Radarsat: 24 days). To differentiate overlapping avalanches a recently developed age-tracking algorithm showed promising results (Eckerstorfer et al., 2019).

6.2 Optical mapping vs. radar change detection

Regardless of the advantages of radar change detection, the spatial resolution of optical sensors is better compared to the nominal resolution of radar sensors because the intrinsically coherent SAR imaging method makes radar speckle unavoidable and requires spatial or temporal averaging. Furthermore, the resolution of TSX and S1 is not good enough to recognize flow structures of the avalanche surface which are well visible in the optical SPOT-6 images (Bühler et al., 2019).

Nevertheless, using TSX change detection we have mapped a similar number of avalanches (316) compared to the results from optical SPOT-6 images (286 avalanches) within the study area. However, the mapped avalanche outlines differ relatively strongly and are sometimes split up into sub-polygons which results in the fact that only 68% of the radar detected avalanches overlap with avalanches found with the optical data or inversely, only 44% of optically detected avalanches were also found by radar. The differences of avalanche outlines could also be partially attributed to the fact that some avalanche outlines were estimated by the (different) persons mapping the avalanches.

The fact that a larger fraction (68% vs. 44%) of radar-detected avalanches matches with optically detected ones results from the better differentiation of adjacent avalanches into multiple classes (*new, old, unsure*) which were often mapped as one large avalanche with optical data. When multitemporal optical data is available, a temporal differentiation is also possible (Bühler et al., 2019) which, however, was done for a different region than our analyzed area.

From the analysis of avalanches detected by radar but not found in the optical SPOT-6 image, we found that more than 80% of these avalanches were located in the cast shadow. Similar, in radar images no information is available from the radar shadow and very poor information is available from layover areas, however, only 35% of avalanches not found in the radar images (but in optical) are located in the radar shadow or layover. We think it is an important result that not only radar acquisitions are affected by (radar) shadow but that avalanche mapping using optical data seem also to be deteriorated by the cast shadow from high mountains.

A main difference between SPOT-6 and radar mapping results is that the total avalanche area differed at least by a factor of three (Fig. 10b). We attribute this difference to the fact with SPOT-6 avalanches were mapped more completely (origin, path, deposition zone) than with radar (mainly deposition zone). This has important consequences when comparing avalanches by pixel area rather than by overlap.

Due to unfortunate acquisition timing, the direct comparison of SPOT-6 and TSX data is not ideal: the SPOT-6 images (2018-01-24) was acquired just between the two TSX images (2018-01-11, 2018-02-02) which leaves 9 days where additional avalanches could have occurred, considering about 20 cm of fresh snow on Feb 1st. Nevertheless, Fig. 2 indicates that the biggest part of avalanches occurred before the SPOT-6 acquisition and only about 5% of avalanches occurred until Feb 2nd. We confirm this by analyzing a multiorbital S1 change detection image S1(01-24+01-28 / 01-30+02-03) where we did not find any new avalanches in the study area.

6.3 TSX compared to S1 change detection

The comparison of TSX and S1 change detection images, both of them acquired for the first avalanche period with almost identical orbits and acquisition times, shows that the S1 satellites are a valuable source of radar images for avalanche mapping. The size of smallest detectable avalanches for TSX are "medium" avalanches (500 – 10 000 m^2) with a width of more than 20 m. S1 misses mainly "medium" avalanches smaller than 2 000 m^2 (Fig. 10b). Similar results for S1 with a minimum cutoff of 4 000 m^2 were found by Eckerstorfer et al. (2019).

Still about two thirds of avalanches detected and classified as *new* with TSX could also be detected with S1 (Sect. 5.3). Notably, 93% (83/89) of avalanches detected by S1 could also be detected by TSX which reflects the agreement between TSX

and S1 mapping results. This is confirmed by Fig. 10b which shows that, despite of a different lower cut off, the total area of radar-mapped *new* avalanches agrees very well ($2.5 \cdot 10^6$ m^2). Also, the shape of the avalanches masked in S1 data is very similar to the one from TSX (Fig. 6). Therefore, we consider the reduced resolution and separability of avalanches in S1 images to be much less relevant than the superior availability of S1 data.

6.4 Multiorbital composite

The combination of radar images acquired with different polarizations and from ascending and descending orbits reduced radar speckle and minimized areas affected by layover. By combining two orbit and (pairwise incoherent) polarizations, areas visible from both orbits were imaged by 4 independent observations. In our case of mapping entire Switzerland for a specific period, this number was even increase to 6 or 8 observations when acquisitions with different incidence angles (from the same orbit direction) overlap. Due to the 4–8 independent observations, spatial multilooking (used for speckle reduction) could be reduced to 4×1 pixels to obtain a radiometric accuracy otherwise only possible with multilooking windows of $8...16 \times 2$ pixels. With this multiorbital averaging method, we estimate that an effective spatial resolution of about 20×20 m was achieved (TSX: about 10×10 m after multilooking). This resolution enhancement can be clearly observed when comparing Fig. 4b with Fig. 4c. Also, about twice as much medium size avalanches were detected compared to a single S1 image (Fig. 10a). However, because topography was not considered during averaging the resolution can deteriorate in slopes facing off the radar (Sect. 3).

Another drawback of combining acquisitions from multiple dates is that no unique time stamp can be given to the "before"- and "after"-aquisition. In the worst case, avalanches loose contrast if they had occurred during the collection period of the set of "before" images. However, in our case, we focused on the extreme avalanche event on 2018-01-04 (Fig. 2) and made sure that the "before"- and "after"-imaging period did not overlap with the main avalanche event. For an operational use combined (asc+desc) acquisitions must be acquired within a time-period as short as possible, i.e. significantly shorter than the orbit revisit time to avoid reduced visibility by averaging out "in-between" avalanches which are only visible in one of the two averaged acquisitions. For S1, ascending and descending acquisitions with only 12 hours time difference should be used, if possible. Considering a revisit time of 6 days over Europe results in probability of 1:12 to reduce the visibility of averaged avalanches.

In this study we simply averaged the change detection radar images and did not apply any terrain correction. We think that more advanced methods to merge radar images from multiple orbits, for example local resolution weighting (LRW) by Small (2012), should further improve avalanche mapping results. From the comparison to optical data we also found that avalanches can be clearer identified in slopes facing off the radar compared to slopes which are facing towards the radar (but not yet in layover). As detailed in Sect. 3, we think that, because of the more isotropic scattering from the rough avalanche debris surface, steep local radar incidence angles should be used to enhance the local contrast to the surrounding snow. Therefore, slopes facing away from the sensor should be given more weight which is done already implicitly by LRW. Furthermore, in mountainous regions LRW applies already unequal weights for ascending and descending acquisitions which decreases further the probability that avalanche falling inbetween the averaged acquisitions loose their visibility.

Table 7. Avalanche differentiation ratios between different satellite acquisitions and methods, and mutual miss-/false discovery rates.

Set A	Set B	$\frac{N_{A\to B}}{N_{B\to A}}$	$\frac{N_{A\neg B}}{N_A}$	$\frac{N_{B\neg A}}{N_B}$
tsx(12-31 / 01-11)	SPOT-6 (01-24)	1.72	32%	56%
tsx(12-31 / 01-11)	S1(12-31 / 01-12)	1.25	37%	7%
tsx(12-31 / 01-11)	S1-MO	1.06	33%	24%
tsx(12-31 / 01-11)	manual vs. auto	0.94	33%	15%
S1(12-31 / 01-12)	manual vs. auto	0.94	24%	22%
tsx(01-11 / 02-02)	manual vs. auto	0.66	52%	30%

6.5 Automated avalanche detection

For both, TSX and S1 images the implemented avalanche detection algorithm performs with reasonable results, at least when the number of overlapping avalanches is low. That means that in general a few sparse events are more likely to be detected than overlapping clusters of avalanches.

Compared to the manually detected avalanches (red shading in Fig. 9), the area of automatically detected avalanches (yellow) shows a good agreement. However, the upslope parts of avalanches are often only fractionally detected because of their relatively low brightness. For a weakly visible starting or transition zone a human observer can conclude that it must belong to the below situated avalanche deposit. Also, by choosing a threshold of 4 dB already 18 % of the manually detected avalanches are likely to be missed (Fig. 8a). A dynamic threshold based on backscatter changes in individual image pairs could improve these results (Eckerstorfer et al., 2019). Further, minor parts of manually detected avalanches are located in slopes steeper than 35° (Fig. 8b) which were masked out by the automatic method.

6.6 Avalanche differentiation with different methods

The fact that no real ground truth exists makes a direct comparison of the different methods difficult. However, some methods show a much higher potential to differentiate large connected avalanche patches into multiple smaller ones than other methods. Therefore we use a reciprocal, two-way comparison of avalanche detection numbers to estimate which of the methods can better differentiate adjacent avalanches.

As a proxy for the enhanced differentiation we define the ratio $N_{A\to B}/N_{B\to A}$ where $N_{A\to B}$ is the number of avalanches from data set A which were also found in the data set B, and inversely, $N_{B\to A}$ is the number of avalanches in B which were also found in A. Additionally, we define the ratio $N_{A\neg B}/N_A$ of avalanches found in A but not found in B relative to all avalanches found in A and analogue $N_{B\neg A}/N_B$. The meaning of the last two ratios depends on interpretation and correspond to the false discovery rate (FDR) under the assumption that B is considered as truth or alternatively to the false negative rate (FNR) if A is considered as truth.

Table 7 lists the three ratios for different data sets. We interpret these numbers such that a differentiation ratio $\frac{N_{A\to B}}{N_{B\to A}} > 1$ indicates that set A provides spatially more detailed results than set B. An asymmetry between the last two columns indicates that one method detects more avalanches than the other method.

From the comparison to SPOT-6, derived from Table 3, we infer that TSX change detection allows for a better differentiation of avalanches than single optical images. However, both methods show miss rates (and possibly some false detection) of 32 and 56% for avalanches which are not visible by the other method which indicates a certain complementarity of optical and radar images for avalanche detection.

Compared to S1, the higher resolution of TSX allows for a 25% better differentiation and 37% more avalanches were detected (derived from Table 4). Still, the false discovery rate of S1 compared to TSX is quite low (7%).

Interestingly, the avalanche separability of the multiorbital S1 composite, including the NL mean filter, is very comparable to TSX single orbit change detection (1.06) while 33% or 24% of avalanches detected by one method are not visible with the other (derived from Table 5). This, because TSX detects smaller avalanches, while the multiorbital methods detects also avalanches which are otherwise in slopes close to layover.

Finally, the automatic methods detect larger avalanches fairly comparably to the manual method (derived from Table 6), however, weakly visible avalanches and small avalanches which have not been automatically detected cause a miss rate of about 30 %. The apparently lower differentiation of avalanche by manual analysis results from the fact that the automatic method often detects multiple patches instead of a single avalanche (Fig. 9).

7 Conclusions

We studied the capabilities of the radar satellites TerraSAR-X (TSX) and Sentinel-1 (S1) to detect avalanches in two-image change detection images and multiorbital change detection composites. Manual avalanche mapping results from the high- and medium resolution radar data (TSX, S1) and high resolution optical data (SPOT-6) were compared to each other. An automatic detection method was developed and compared to the manual mapping results.

We conclude that both, TSX and S1 radar images can provide valuable, weather-independent information about avalanche activity, even in difficult alpine terrain. Despite of different lower cut-off sizes of about 500 m^2 for TSX and 2000 m^2 for S1, avalanche outlines and the total area of mapped avalanches agree very well with each other.

Between the manual TSX and SPOT-6 mapping results, we found a fair agreement but the total mapped avalanche area of TSX covers only one third (the deposition zone) of the total mapped area (release, path, deposit) in SPOT-6 images. Interestingly, many avalanches located in the cast shadow of SPOT-6 image were not detected whereas they were clearly visible in a TSX image acquired 10 days later. With the automated detection algorithm we found about 60–80% of the avalanches manually mapped in the same image, at least when no large number of old avalanches were present.

We found that the non-systematic acquisition program and the possibly high cost can be considered as drawback of TSX data. Also, with the maximal swath width of 30 km in stripmap mode and a nominal revisiting period of 11 days, an operational use for avalanche mapping over Switzerland with TSX is not feasible. However, the high resolution images can provide valuable

information for validation of lower resolution mapping results for pre-defined test sites and if acquisitions are scheduled in advance.

Despite of the lower resolution, we found that S1 provides a convincing solution for systematic avalanche mapping because of the total swath width of 250 km and the revisit period of 6 days when images from the same orbit of both satellites (S1-A and S1-B) are combined. The results from Norway by Eckerstorfer et al. (2018, 2019) confirm this conclusion.

With the multiorbital combination of systematically available S1 acquisitions from different orbits and with different polarizations we minimized not only areas located in radar layover but also enhanced the radiometric accuracy and obtained a high spatial resolution of about 20×20 m. In the resulting change detection image covering entire Switzerland we manually counted in total 7361 new avalanches which occurred during an extreme avalanche period around January 4$^{\text{th}}$ 2018. However, we suppose that mainly avalanches reaching below the wet snow line were detected and that likely many dry snow avalanches were missed because of their lower contrast to the surrounding snow. A disadvantage of the multiorbital composite is the loss of precise timing of avalanches. For operational applications we suggest therefore to minimize the ratio of elapsed time between ascending and descending acquisitions and of the revisit time.

We think that avalanche mapping can be further improved with more advanced methods to combine different orbits, for example with local resolution weighing, LRW (Small, 2012). With that, slopes facing off the radar are weighted stronger which does not only enhance the resolution but should also increase the avalanche visibility: we think that the more omnidirectional scattering of the rough avalanche surface dominates the scattering of smooth snow only for slopes facing off the radar. We found that avalanches are hardly visible in slopes facing the radar (but not yet in layover). As with LRW mountain slopes are unequally weighted the probability that avalanches occur between two averaged images is reduced.

Although we could show that radar change detection mapping with TSX provides results comparable to optical SPOT-6 direct mapping, we note that our study focuses on the exceptionally warm January 2018 with frequent surface melt but also with very intense snowfall periods. As the relative brightness of avalanches with respect to the surrounding snow depends on the water content and the amount of deposited snow, avalanches might be less visible during cold weather with little snowfall. Therefore, we think that an analysis of longer time series of radar based avalanche mapping will provide insight how snow and weather conditions affect the detection rate of radar based methods.

Data availability. TerraSAR-X data are available from the archive https://terrasar-x-archive.terrasar.com. Copernicus Sentinel-1 data processed by ESA have been downloaded from the Copernicus Open Access Hub: https://scihub.copernicus.eu and from the Alaska SAR Facility ASF DAAC 2018 https://www.asf.alaska.edu. The manual mapping results from the optical data and the Sentinel-1 change detection composite of Switzerland is available online (Hafner and Bühler, 2019; Leinss et al., 2019).

Table A1. List of S1 acquisitions used for the multiorbital RGB change detection composite shown in Fig. 7.

Satellite	Date	Time (UTC)	rel. orbit, direction
Sentinel-1B	2017-12-28	05:42:17	139, descending
Sentinel-1B	2017-12-28	05:42:43	139, descending
Sentinel-1A	2017-12-29	05:34:45	66, descending
Sentinel-1A	2017-12-29	05:35:10	66, descending
Sentinel-1B	2017-12-30	05:26:02	168, descending
Sentinel-1B	2017-12-30	05:26:27	168, descending
Sentinel-1A	2017-12-30	17:23:14	88, ascending
Sentinel-1A	2017-12-30	17:23:39	88, ascending
Sentinel-1B	2017-12-31	17:14:13	15, ascending
Sentinel-1B	2017-12-31	17:14:38	15, ascending
Sentinel-1A	2018-01-01	17:06:47	117, ascending
Sentinel-1A	2018-01-01	17:07:12	117, ascending
Sentinel-1B	2018-01-09	05:42:17	139, descending
Sentinel-1B	2018-01-09	05:42:42	139, descending
Sentinel-1A	2018-01-10	05:34:45	66, descending
Sentinel-1A	2018-01-10	05:35:10	66, descending
Sentinel-1B	2018-01-11	05:26:01	168, descending
Sentinel-1B	2018-01-11	05:26:26	168, descending
Sentinel-1A	2018-01-11	17:23:14	88, ascending
Sentinel-1A	2018-01-11	17:23:39	88, ascending
Sentinel-1B	2018-01-12	17:14:13	15, ascending
Sentinel-1B	2018-01-12	17:14:38	15, ascending
Sentinel-1A	2018-01-13	17:06:47	117, ascending
Sentinel-1A	2018-01-13	17:07:12	117, ascending

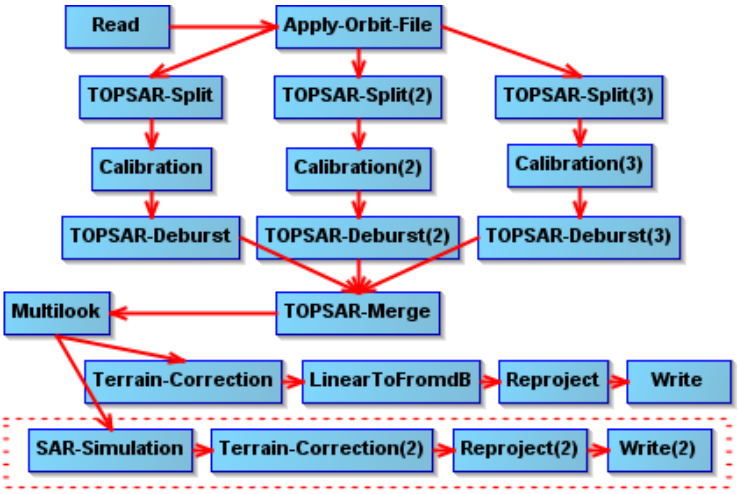

Figure A1. SNAP workflow to process S1 data. The red dashed box is used for creation of the layover and shadow map.

Appendix A

Author contributions. SL and RW wrote the manuscript, RW did the avalanches mapping and designed the automatic detection. SL coordinated the study and implemented the nonlocal mean filter. SH, SB, SL preprocessed the radar images. YB initiated the study and complemented the manuscript.

Competing interests. The authors declare that they have no conflict of interest.

Acknowledgements. We thank Elisabeth Hafner from SLF for providing the manual avalanche mask from the optical SPOT-6 data. Lanqing Huang assisted SH to process the S1 data. We are deeply grateful to Irena Hajnsek from ETH Zürich for providing the working environment, the computational resources and her interest for this work. TerraSAR-X data are provided by the German Aerospace Center (Proposal ID: LAN3585). Meteorological data are provided by the Swiss Federal Office of Meteorology and Climatology (MeteoSwiss).

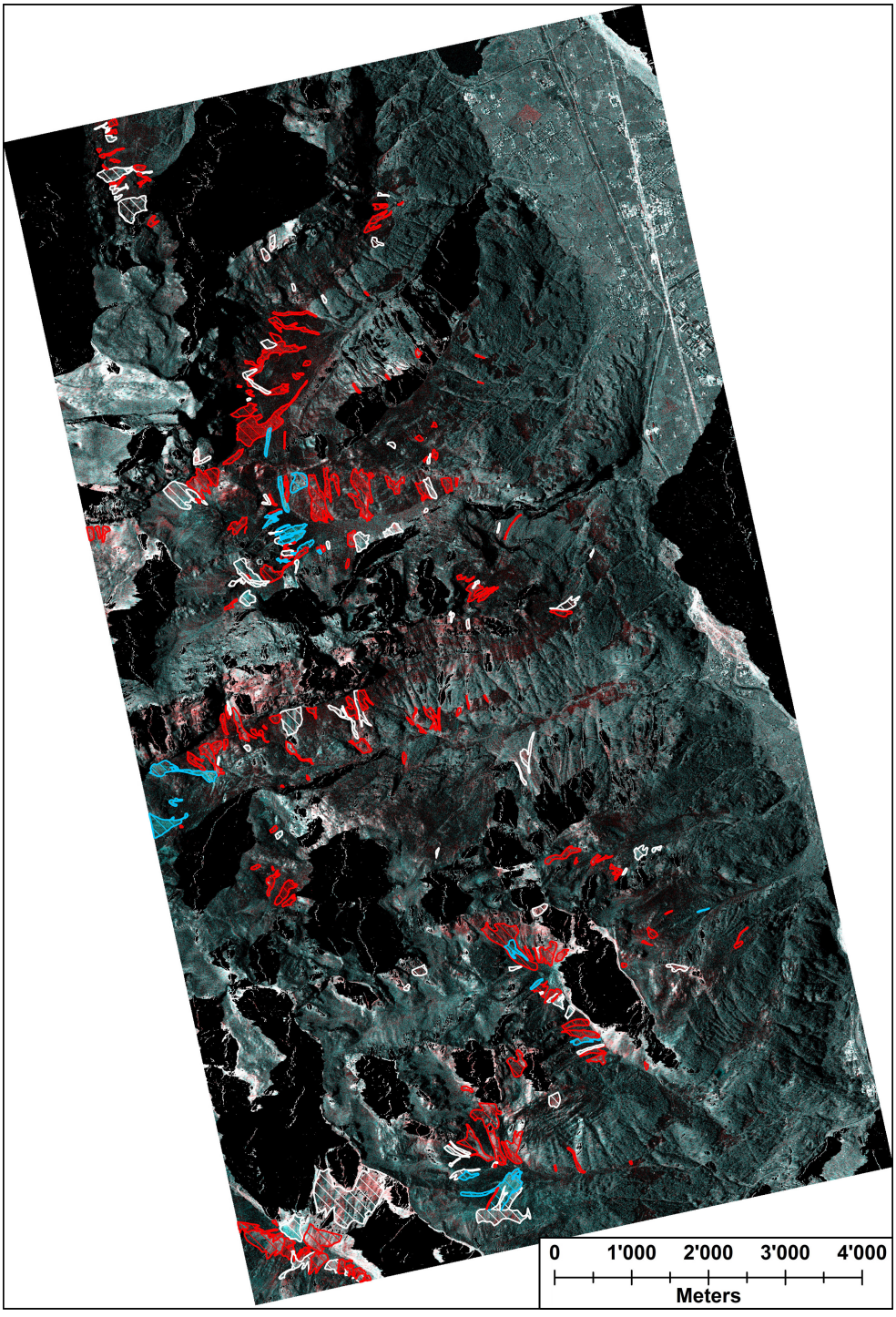

Figure A2. Full extent of the RGB composite image TSX 2017-31-12 vs. 2018-01-11 with manually mapped avalanches. *New* avalanches are red, *old* avalanches blue and *unsure* avalanches white. Areas in the radar layover and shadow are masked out (black). TerraSAR-X image orthorectified with the swissALTI3D © 2019 swisstopo (JD100042), reproduced with the authorisation of swisstopo (JA100120).

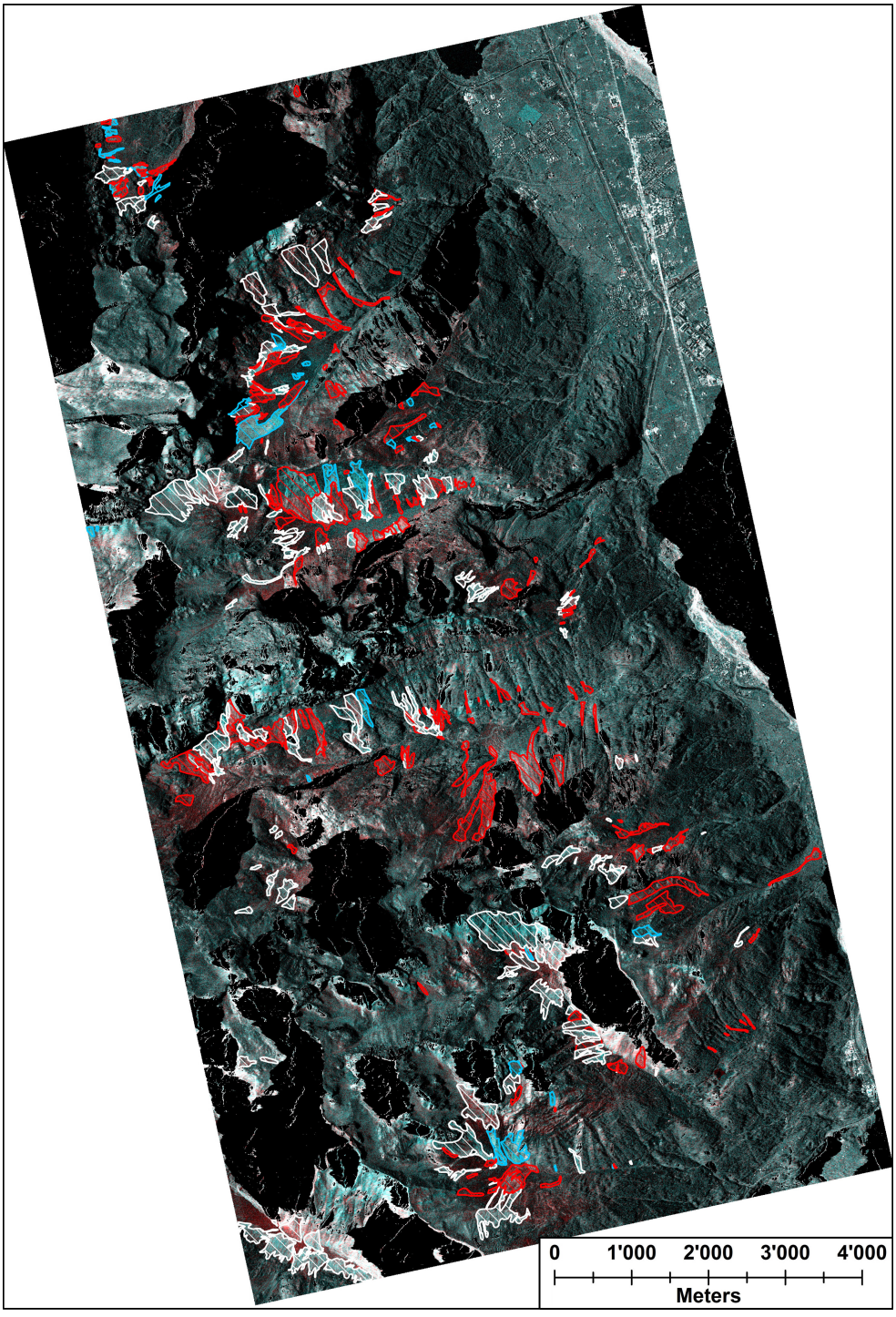

Figure A3. Full extent of the RGB composite image TSX 2018-01-11 vs. 2018-02-02 with manually mapped avalanches. *New* avalanches are red, *old* avalanches blue and *unsure* avalanches white. Areas in the radar layover and shadow are masked out (black). TerraSAR-X image orthorectified with the swissALTI3D © 2019 swisstopo (JD100042), reproduced with the authorisation of swisstopo (JA100120).

References

Abermann, J., Eckerstorfer, M., Malnes, E., and Hansen, B. U.: A large wet snow avalanche cycle in West Greenland quantified using remote sensing and in situ observations, Natural Hazards, 97, 517–534, https://doi.org/10.1007/s11069-019-03655-8, 2019.

Bühler, Y., Hüni, A., Meister, R., Christen, M., and Kellenberger, T.: Automated detection and mapping of avalanche deposits using airborne optical remote sensing data, Cold Regions Science and Technology, 57, 99–106, https://doi.org/10.1016/j.coldregions.2009.02.007, 2009.

Bühler, Y., Hafner, E. D., Zweifel, B., Zesiger, M., and Heisig, H.: Where are the avalanches? Rapid SPOT6 satellite data acquisition to map an extreme avalanche period over the Swiss Alps, The Cryosphere, 13, 3225–3238, https://doi.org/10.5194/tc-13-3225-2019, 2019.

Bühler, Y., Bieler, C., Pielmeier, C., Frauenfelder, R., Jaedicke, C., Schwaizer, G., Wiesmann, A., and Caduff, R.: Final Report: Improved Alpine Avalanche Forecast Service AAF, techreport, European Space Agency ESA, 2014.

Condat, L.: A Simple Trick to Speed Up the Non-Local Means, https://hal.archives-ouvertes.fr/hal-00512801, working paper or preprint, 2010.

Cumming, W. A.: The Dielectric Properties of Ice and Snow at 3.2 Centimeters, Journal of Applied Physics, 23, 768–773, https://doi.org/10.1063/1.1702299, 10.1063/1.1702299, 1952.

Di Tommaso, P., Floden, E. W., Barja, P. P., Palumbo, E., and Notredame, C.: Nextflow enables reproducible computational workflows, Nature Biotechnology, 35, 316–319, https://doi.org/10.1038/nbt.3820, 2017.

Eckerstorfer, M. and Malnes, E.: Manual detection of snow avalanche debris using high-resolution Radarsat-2 SAR images, Cold Regions Science and Technology, 120, 205 – 218, https://doi.org/10.1016/j.coldregions.2015.08.016, http://www.sciencedirect.com/science/article/pii/S0165232X15002037, 2015.

Eckerstorfer, M., Bühler, Y., Frauenfelder, R., and Malnes, E.: Remote sensing of snow avalanches: Recent advances, potential, and limitations, Cold Regions Science and Technology, 121, 126–140, https://doi.org/10.1016/j.coldregions.2015.11.001, 2016.

Eckerstorfer, M., Malnes, E., and Müller, K.: A complete snow avalanche activity record from a Norwegian forecasting region using Sentinel-1 satellite-radar data, Cold Regions Science and Technology, 144, 39–51, https://doi.org/10.1016/j.coldregions.2017.08.004, international Snow Science Workshop 2016 Breckenridge, 2017.

Eckerstorfer, M., Malnes, E., Vickers, H., Müller, K., Engeset, R., and Humstad, T.: Operational avalanche activity monitoring using radar satellites: From Norway to worldwide assistance in avalanche forecasting, in: International Snow Science Workshop, At Innsbruck, Austria, 2018.

Eckerstorfer, M., Vickers, H., Malnes, E., and Grahn, J.: Near-Real Time Automatic Snow Avalanche Activity Monitoring System Using Sentinel-1 SAR Data in Norway, Remote Sensing, 11, https://doi.org/10.3390/rs11232863, 2019.

ESA: Sentinel-1: ESA's Radar Observatory Mission for GMES Operational Services (ESA SP-1322/1, March 2012), Tech. rep., ESA, 2012.

Frauenfelder, R., Malnes, E., Solberg, R., and Müller, K.: Towards an automated snow property and avalanche mapping system (ASAM), techreport 20130092-04-R, Norwegian Geotechnical Institute NGI, 2015.

Fung, A. K. and Eom, H. J.: Application of a Combined Rough Surface And Volume Scattering Theory to Sea Ice And Snow Backscatter, IEEE Transactions on Geoscience and Remote Sensing, GE-20, 528–536, 1982.

Hafner, E. and Bühler, Y.: SPOT6 Avalanche outlines 24 January 2018, https://doi.org/10.16904/envidat.77, 2019.

Hamar, J. B., Salberg, A., and Ardelean, F.: Automatic detection and mapping of avalanches in SAR images, in: 2016 IEEE International Geoscience and Remote Sensing Symposium (IGARSS), pp. 689–692, https://doi.org/10.1109/IGARSS.2016.7729173, 2016.

International Commission of Snow and Ice: Avalanche atlas: illustrated international avalanche classification, Unesco Paris, https://unesdoc.unesco.org/ark:/48223/pf0000048004, 1981.

Jin, Q., Grama, I., and Liu, Q.: Removing Gaussian Noise by Optimization of Weights in Non-Local Means, 2012 Symposium on Photonics and Optoelectronics, SOPO 2012, https://doi.org/10.1109/SOPO.2012.6270436, 2011.

Karbou, F., Coléou, C., Lefort, M., Deschatres, M., Eckert, N., Martin, R., Charvet, G., and Dufour, A.: Monitoring avalanche debris in the French mountains using SAR observations from Sentinel-1 satellites, in: Proceedings of the International Snow Science Workshop, 1, pp. 344–347, 2018.

Kendra, J. R., Sarabandi, K., and Ulaby, F. T.: Radar measurements of snow: experiment and analysis, IEEE Transactions on Geoscience and Remote Sensing, 36, 864–879, 1998.

Korzeniowska, K., Bühler, Y., Marty, M., and Korup, O.: Regional snow-avalanche detection using object-based image analysis of near-infrared aerial imagery, Nat. Hazards Earth Syst. Sci., 17, 1823–1836, https://doi.org/10.5194/nhess-17-1823-2017, 2017.

Lato, M. J., Frauenfelder, R., and Bühler, Y.: Automated detection of snow avalanche deposits: segmentation and classification of optical remote sensing imagery, Natural Hazards and Earth System Sciences, 12, 2893–2906, https://doi.org/10.5194/nhess-12-2893-2012, 2012.

Leader, J.: The relationship between the Kirchhoff approach and small perturbation analysis in rough surface scattering theory, IEEE Transactions on Antennas and Propagation, 19, 786–788, 1971.

Leinss, S., Wiesmann, A., Lemmetyinen, J., and Hajnsek, I.: Snow water equivalent of dry snow measured by differential interferometry, IEEE J. Sel. Topics Appl. Earth Observ. Remote Sens., 8, 3773–3790, https://doi.org/10.1109/JSTARS.2015.2432031, 2015.

Leinss, S., Holenstein, S., and Wicki, R.: Sentinel-1 change detection mosaic of Switzerland for the avalanche event of January 4th 2018, https://doi.org/10.3929/ethz-b-000376048, 2019.

Matzler, C.: Microwave permittivity of dry snow, IEEE Transactions on Geoscience and Remote Sensing, 34, 573–581, 1996.

Meister, R.: Country-wide avalanche warning in Switzerland, in: Proceedings International Snow Science Workshop, Snowbird, Utah, USA, 30 October-3 November 1994, pp. 58–71, ISSW 1994 Organizing Committee Snowbird UT, USA, 1995.

Rignot, E., Echelmeyer, K., and Krabill, W.: Penetration depth of interferometric synthetic-aperture radar signals in snow and ice, Geophysical Research Letters, 28, 3501–3504, https://doi.org/10.1029/2000GL012484, 2001.

Rudolf-Miklau, F., Sauermoser, S., Mears, A., and Boensch, M.: The Technical Avalanche Protection Handbook, Wiley, 2014.

Schweizer, J., Jamieson, J. B., and Skjonsberg, D.: Avalanche forecasting for transportation corridor and backcountry in Glacier National Park (BC, Canada), 25 Years of Snow Avalanche Research, Voss, Norway, 12-16 May 1998, pp. 238–243, 1998.

Schweizer, J., Kronholm, K., and Wiesinger, T.: Verification of regional snowpack stability and avalanche danger, Cold Regions Science and Technology, 37, 277 – 288, https://doi.org/https://doi.org/10.1016/S0165-232X(03)00070-3, http://www.sciencedirect.com/science/article/pii/S0165232X03000703, iSSW 2002: International Snow Science Workshop, 2003.

Scott, D.: Avalache Mapping: GIS for Avalanche Studies and Snow Science, The Avalanche Review, 27, 20–21, 2009.

SLF: Wochenbericht 05. Januar – 11. Januar 2018, https://www.slf.ch/de/lawinenbulletin-und-schneesituation/wochen-und-winterberichte/201718/wob-05-11-januar.html, 2018a.

SLF: Wochenbericht 12.–18. Januar 2018, https://www.slf.ch/de/lawinenbulletin-und-schneesituation/wochen-und-winterberichte/201718/wob-12-18-januar.html, 2018b.

SLF: Wochenbericht 19.–25. Januar 2018, https://www.slf.ch/de/lawinenbulletin-und-schneesituation/wochen-und-winterberichte/201718/wob-19-25-januar.html, 2018c.

SLF: Wochenbericht 26. Januar–01. Februar 2018, https://www.slf.ch/de/lawinenbulletin-und-schneesituation/wochen-und-winterberichte/201718/wob-26-januar-01-februar.html, 2018d.

SLF: Avalanche Bulletin, https://www.slf.ch/en/avalanche-bulletin-and-snow-situation.html#avalanchedanger, 2018e.

Small, D.: Flattening Gamma: Radiometric Terrain Correction for SAR Imagery, IEEE Transactions on Geoscience and Remote Sensing, 49, 3081–3093, https://doi.org/10.1109/TGRS.2011.2120616, 2011.

Small, D.: SAR backscatter multitemporal compositing via local resolution weighting, in: 2012 IEEE International Geoscience and Remote Sensing Symposium, pp. 4521–4524, https://doi.org/10.1109/IGARSS.2012.6350465, 2012.

Techel, F., Jarry, F., Kronthaler, G., Mitterer, S., Nairz, P., Pavšek, M., Valt, M., and Darms, G.: Avalanche fatalities in the European Alps: long-term trends and statistics, Geographica Helvetica, 71, 147–159, https://doi.org/10.5194/gh-71-147-2016, 2016.

Tiuri, M., Sihvola, A., Nyfors, E., and Hallikainen, M.: The complex dielectric constant of snow at microwave frequencies, IEEE Journal of Oceanic Engineering, 9, 377–382, https://doi.org/10.1109/JOE.1984.1145645, 1984.

Vickers, H., Eckerstorfer, M., Malnes, E., Larsen, Y., and Hindberg, H.: A method for automated snow avalanche debris detection through use of synthetic aperture radar (SAR) imaging, Earth and Space Science, 3, 446–462, https://doi.org/10.1002/2016EA000168, 2016.

Watte, W. P. and MacDonald, H. C.: Snowfield mapping with K-band radar, Remote Sensing of Environment, 1, 143 – 150, https://doi.org/https://doi.org/10.1016/S0034-4257(70)80016-5, http://www.sciencedirect.com/science/article/pii/S0034425770800165, 1970.

Werninghaus, R. and Buckreuss, S.: The TerraSAR-X mission and system design, Geoscience and Remote Sensing, IEEE Transactions on, 48, 606–614, https://doi.org/10.1109/TGRS.2009.2031062, 2010.

Wesselink, D. S., Malnes, E., Eckerstorfer, M., and Lindenbergh, R. C.: Automatic detection of snow avalanche debris in central Svalbard using C-band SAR data, Polar Research, 36, 1333 236, https://doi.org/10.1080/17518369.2017.1333236, 2017.

Wiesmann, A., Mätzler, C., and Weise, T.: Radiometric and structural measurements of snow samples, Radio Science, 33, 273–289, https://doi.org/10.1029/97RS02746, https://agupubs.onlinelibrary.wiley.com/doi/abs/10.1029/97RS02746, 1998.

Wiesmann, A., Wegmuller, U., Honikel, M., Strozzi, T., and Werner, C. L.: Potential and methodology of satellite based SAR for hazard mapping, in: IGARSS 2001. Scanning the Present and Resolving the Future. Proceedings. IEEE 2001 International Geoscience and Remote Sensing Symposium (Cat. No.01CH37217), vol. 7, pp. 3262–3264 vol.7, 2001.

Winkler, K., Zweifel, B., Marty, C., and Techel, F.: Schnee und Lawinen in den Schweizer Alpen, Hydrologisches Jahr 2017/18, WSL Berichte, 77, 2019.

Xu, X., Tsang, L., and Yueh, S.: Electromagnetic Models of Co/Cross Polarization of Bicontinuous/DMRT in Radar Remote Sensing of Terrestrial Snow at X- and Ku-band for CoReH2O and SCLP Applications, IEEE Journal of Selected Topics in Applied Earth Observations and Remote Sensing, 5, 1024–1032, 2012.